Biomaterials 32 (2011) 3700–3711

Contents lists available at ScienceDirect

Biomaterials

journal homepage: www.elsevier.com/locate/biomaterials

Engineering the cell–material interface for controlling stem cell adhesion, migration, and differentiation

Ramses Ayala [a], Chao Zhang [a], Darren Yang [b], Yongsung Hwang [a], Aereas Aung [a], Sumeet S. Shroff [a], Fernando T. Arce [a], Ratnesh Lal [a], Gaurav Arya [b], Shyni Varghese [a,*]

[a] Department of Bioengineering, University of California San Diego, 9500 Gilman Drive, MC 0412, La Jolla, CA 92093, United States
[b] Department of Nanoengineering, University of California San Diego, 9500 Gilman Drive, MC 0448, La Jolla, CA 92093, United States

ARTICLE INFO

Article history:
Received 18 January 2011
Accepted 1 February 2011
Available online 10 March 2011

Keywords:
Mesenchymal stem cells
Stem cell differentiation
Cell migration
Cytoskeletal organization
Hydrogel matrices
Hydrophobicity

ABSTRACT

The effective utilization of stem cells in regenerative medicine critically relies upon our understanding of the intricate interactions between cells and their extracellular environment. While bulk mechanical and chemical properties of the matrix have been shown to influence various cellular functions, the role of matrix interfacial properties on stem cell behavior is unclear. Here, we report the striking effect of matrix interfacial hydrophobicity on stem cell adhesion, motility, cytoskeletal organization, and differentiation. This is achieved through the development of tunable, synthetic matrices with control over their hydrophobicity without altering the chemical and mechanical properties of the matrix. The observed cellular responses are explained in terms of hydrophobicity-driven conformational changes of the pendant side chains at the interface leading to differential binding of proteins. These results demonstrate that the hydrophobicity of the extracellular matrix could play a considerably larger role in dictating cellular behaviors than previously anticipated. Additionally, these tunable matrices, which introduce a new control feature for regulating various cellular functions offer a platform for studying proliferation and differentiation of stem cells in a controlled manner and would have applications in regenerative medicine.

1. Introduction

The interaction of stem cells with their surrounding microenvironment is fundamental to multiple processes such as cell migration, proliferation, lineage specificity, and tissue morphogenesis [1–8]. The microenvironment is comprised of the extracellular matrix (ECM), the aqueous milieu enriched with soluble morphogens, and the neighboring cells [2,9]. How the soluble components influence cellular processes has been studied extensively, but it has become clearer only over the last decade or so that the “insoluble” component, the ECM, plays an equally important role in stem cell growth and differentiation [5,7,10–12].

Most studies examining matrices as regulators of stem cell function have attributed the effects of the matrix to their “bulk” mechanical and chemical properties [10,12–14]. However, since cells interact with the matrix through the cell–matrix interface, the “interfacial” properties of the matrix—interfacial energy, hydrophobicity, and surface topography—play an equally important role in regulating stem cell functions. Mei et al. have recently conducted a high throughput analysis examining how various material properties correlate with the adhesion and self-renewal of human embryonic stem cells and found that matrix hydrophobicity exhibits a strong correlation with the observed cellular behaviors [15]. Also, we know that changes in the mechanical or chemical properties of the matrix, which strongly modulate stem cell behavior, could also introduce changes in the interfacial properties, suggesting possible role of interfacial properties co-acting with bulk parameters to modulate cellular functions.

The role of interfacial properties on cellular behaviors is not surprising as almost a century ago D’Arcy Thompson foretold the importance of interfacial properties in dictating cell form and morphogenesis [16,17]. Over the years, interfacial properties have been implicated to play increasingly important roles on a wide spectrum of cellular functions ranging from cell adhesion and mechanics [17–21] to the function of biomolecules [22,23]. However, the role of interfacial properties such as hydrophobicity independent of functional group(s) and mechanical properties on stem cell growth and differentiation has not been examined so far.

One of the major challenges in understanding the effect of matrix interfacial properties has been de-convoluting its effects from those arising due to the bulk properties of the matrix. In this study, we address this issue by developing tunable, synthetic matrices in which

---

[*] Corresponding author. Fax: +1 858 534 5722.
E-mail address: svarghese@ucsd.edu (S. Varghese).

0142-9612/$ – see front matter © 2011 Elsevier Ltd. All rights reserved.
doi:10.1016/j.biomaterials.2011.02.004

the interfacial hydrophobicity is controlled in a systematic manner by varying the alkyl chain length of pendant side chains without altering the chemical functional group and mechanical properties of the matrix. Using these matrices, we demonstrate that the interfacial hydrophobicity of the matrix, which determines how favorably (or unfavorably) the matrix interacts with the aqueous milieu, play a pivotal role in governing adhesion, cytoskeletal organization, migration, and differentiation of human mesenchymal stem cells (hMSCs).

2. Materials and methods

2.1. Synthesis of acryloyl amino acid (AA) monomers

AA monomers were synthesized from the following materials, C1: Glycine (Fisher Scientific); C2: 3-aminopropanoic acid (Acros Organics); C3: 4-aminobutyric acid (Acros Organics); C4: 5-aminovaleric acid (Aldrich); C5: 6-aminocaproic acid (Acros Organics); C6: 7-aminoheptanoic acid (Peptech Corporation); C7: 8-aminocaprylic acid (Acros Organics); C10: 11-aminoundecanoic acid (Aldrich), as described elsewhere [24]. Briefly, 0.1 mol glycine and 0.11 mol NaOH were dissolved in 80 ml deionized water in an ice bath under vigorous stirring. To this, 0.11 mol acryloyl chloride in 15 ml tetrahydrofuran was added drop wise. The pH was maintained at 7.5–7.8 until the reaction was complete. The reaction mixture was then extracted using ethyl acetate. The clear aqueous layer was acidified to pH 2.0 and then extracted with ethyl acetate. The organic layers were collected, combined, and dried over sodium sulfate. The solution was then filtered, concentrated, and precipitated in petroleum ether. Further purification was achieved by repeated precipitation, and the final product was lyophilized. Synthesis of other monomers followed similar procedure, with variations in pH during the acidification: pH 2.0 for C2, and C3; pH 3.0 for C4, C5, and C6; pH 5.0 for C7 and C10.

2.2. Hydrogel preparation

The hydrogels were synthesized by copolymerizing acrylamide (Am) with AA monomers at 7:1, 6:2, 5:3, and 3:5 mol ratios. The monomers were dissolved in a DMSO/water mixture (1:2), and polymerized in BioRad 1 mm spacer glass plates at room temperature using 1% (w/v) bis-acrylamide (cross-linker) and 1% ammonium persulfate/TEMED (initiator/accelerator). In one set of experiments, we polymerized C5 hydrogels in silanized glass to promote collapse of side chains and increase their hydrophobicity. To silanize the glass slides, they were immersed in anhydrous toluene containing chlorotrimethylsilane (3:1 ratio) for 30 min, washed with methanol and toluene, and air-dried. In all experiments, 1 cm^2 hydrogel disks were used. For cell culture experiments, hydrogels were sterilized in 70% ethanol and washed with sterile PBS containing 50 units/ml penicillin/streptomycin, changing buffer every hour. Hydrogel disks were incubated in culture media for 16 h before plating cells. Since the concentration of AA monomers in the hydrogels is very small and all the monomers are completely soluble in the solvent prior to gelation, the hydrogels thus formed is mainly composed of random copolymers [24].

2.3. Monomer and hydrogel characterization

Proton nuclear magnetic resonance spectra (^1H NMR) of monomers were recorded on Varian Mercury-400 spectrometer at 400 MHz. Carbon-13 nuclear magnetic resonance spectra (^{13}C NMR) were recorded on a Varian Mercury-400 spectrometer at 100 MHz; $CDCl_3$ or D_2O were used as solvents. ^{13}C NMR spectra of hydrogels were recorded on a JEOL ECA500 spectrometer at 125.68 MHz using D_2O as a solvent (Figs. S1 and S2).

2.4. Mechanical measurements

The hydrogel rigidity (compressive modulus) was measured using Instron 3342 Universal Testing System (Instron, Norwood, MA, USA) equipped with a Model 2519-104 force transducer [25]. Briefly, equilibrium-swollen hydrogels in PBS were subjected to a maximum force load set to 450 N at a crosshead speed of 10 mm/min. The data acquisition and processing were performed with BlueHill® software. The compressive modulus of the hydrogels was determined by calculating the slope of a linear region of stress–strain curve. Three samples were used to estimate the mechanical properties for each experimental group and results were shown as a mean value with standard deviation.

2.5. Contact angle measurements

The water contact angles of the hydrogels were determined by a sessile drop method at 20 °C using contact angle meter (CAM100, KSV Instruments Ltd.). A 5 μl droplet of water was placed on the surface of hydrogels. All samples were prepared as triplicates and results were shown as a mean value with standard deviation.

2.6. Surface characterization

Surface roughness was characterized using a Multimode AFM equipped with a Nanoscope IIIA controller from Veeco Instruments (Santa Barbara, CA) run by Nanoscope software v5.30. AFM images were acquired in contact mode at forces of ~4 nN with an "E" scanner (maximum scan area 12 × 12 mm^2, from Veeco) using Si_3N_4 cantilevers (Veeco) with 0.06 N/m nominal spring constants. The data was acquired in a 1× PBS buffer solution. Gel samples were typically stored at 37 °C between 1 and 5 days in an incubator before imaging. No significant difference in sample morphology was noticed as a function of incubation time. The PBS solution was changed 4 times before imaging to remove possible contaminants. For a given scan area, the reported roughness value is the average root mean square (RMS) roughness obtained from two different spots of triplicate specimens. Data was analyzed using the nanoscope software. Using the manufacturer's software, flattening order 3 was applied to all images to correct for tilt and bow before roughness analysis.

2.7. Culture of hMSCs

hMSCs (p7043L, Tulane University) were expanded in growth medium (αMEM, 10% fetal bovine serum, 2 mM glutamine, and 50 units/ml penicillin/streptomycin). Fourth passage (P4) hMSCs were used for all the experiments.

2.8. Time-lapse video analysis

Time-lapse video was captured on a Nikon Ti-E microscope, equipped with an environmental control incubator (In vivo Scientific). Images were captured every 5 min for 19 h on the fourth day after plating. Temperature and CO_2 were maintained at 37 °C and 5%. Video and image analysis were performed with ImageJ (NIH). From each video, x/y coordinates of the cell nuclei were noted for ten cells, in 10 min intervals, and normalized to a common point of origin. Total distance traveled was calculated as the cumulative distance regardless of the direction of movement. Experiments were done in duplicate.

2.9. Cell count and surface area analysis

Three images from different fields of view were captured per hydrogel. The total number of adherent cells in each field was counted and averaged per hydrogel. The surface area of ten cells, chosen at random from each field, was measured. In each experiment, three hydrogel samples per hydrogel group were analyzed. All experiments were done in triplicate.

2.10. Shear force assay

We used a modified flow chamber system, which permits hydrogels to be placed in the center and sealed with a glass slide. Laminar flow was applied using a SVP4 peristaltic pump (Stenner) for 15 s after which cells were imaged and flow rate was increased. The stress on the cells was calculated using the Navier–Stokes equation for a Couette Flow between two parallel plates: $\tau\ (\mathrm{dynes/cm^2}) = Q\mu/10wh^2$, where Q is flow rate (ml/min), μ is viscosity (cP), w and h are width and height (cm) of the flow area. The force required to detach a cell was then calculated as the measured stress multiplied by the cell surface area.

2.11. Protein adsorption analysis

Protein adsorption to hydrogels from the serum was determined using Western blot analysis. The hydrogels were incubated for 4 h in FBS. Adsorbed proteins were eluted from the gel by incubating in 100 μl of 2× SDS protein sample buffer (BioRad) for 30 min at 37 °C. Protein samples were analyzed by Western blot using anti-fibronectin (BD Biosciences), anti-laminin β-2 (Santa Cruz), anti-vitronectin (Millipore), anti-fibrinogen γ (Santa Cruz), and anti-collagen I (Fitzgerald) antibodies.

2.12. Surface coverage calculations

The surface coverage of hydrogels with fibronectin (FN) molecules was calculated from quantitation of western blot images. The surface coverage, S, is defined as the area covered by FN molecules adsorbed on a hydrogel: $S = aN_{av}\sigma/2$, where a is the area of the extended FN molecule (140 nm × 2 nm), N_{av} is the Avogadro number, and σ is the calculated amount of adsorbed FN in moles. σ was calculated by incubating hydrogels with 50 μg/ml of FN in PBS for 4 h at 37 °C. Adsorbed FN was eluted from the gel, as described above and analyzed by Western blot. Quantification was carried out by computer-assisted densitometry against a standard curve. The quantity $aN_{av}\sigma$ is multiplied by 1/2 because the functional FN molecule is a dimer and σ is calculated for the monomer. Experiments were done in triplicate and calculated values were averaged for each hydrogel.

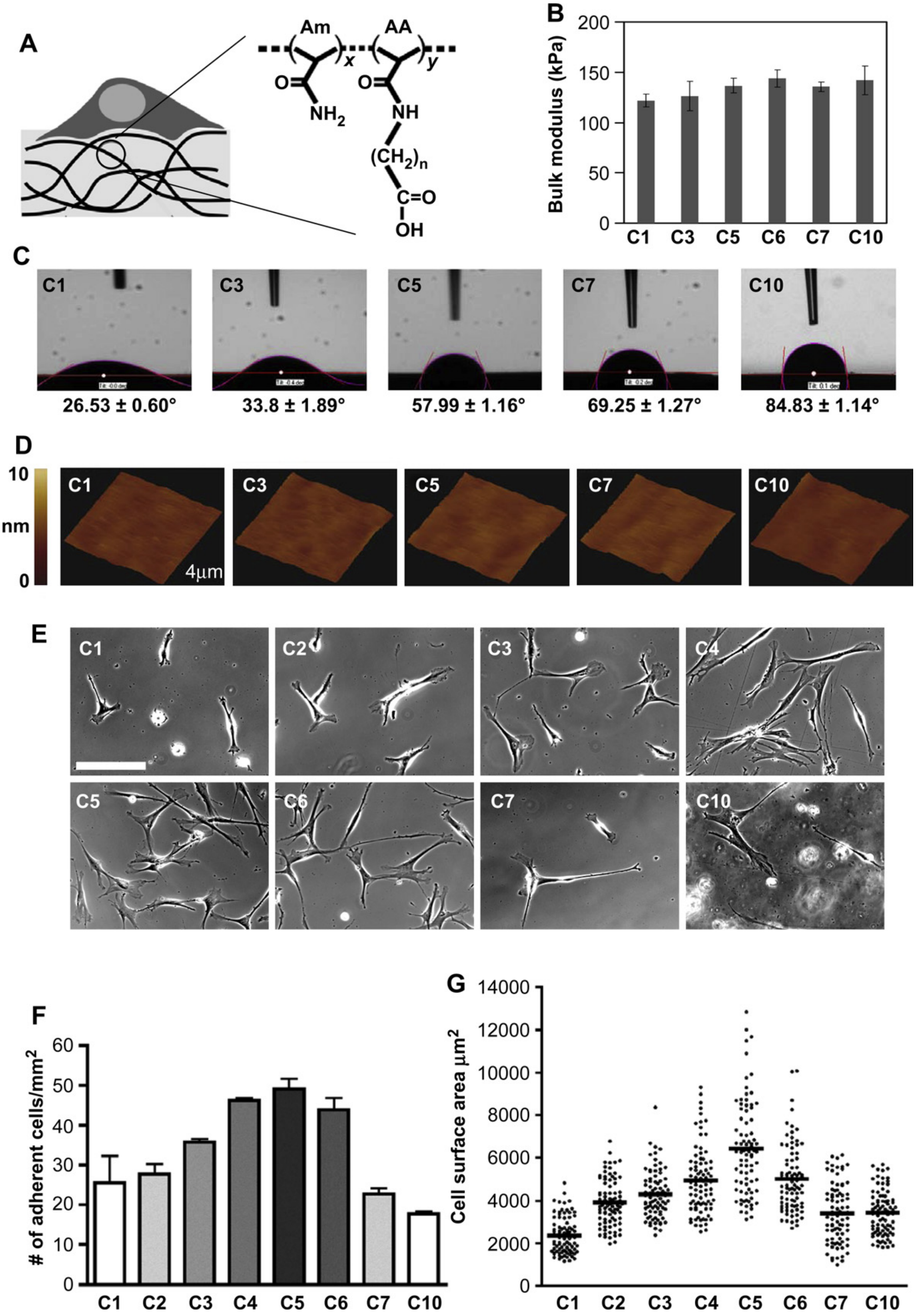

Fig. 1. hMSC cell adhesion and spreading on hydrogels display a non-monotonic dependence on pendant chain hydrophobicity and comonomer concentration. (A) Schematic of hydrogels synthesized from acrylamide (Am) and acryloyl amino acid monomers (AA). The hydrogels are referred to as C1, C2, … C10 depending upon the number of CH_2 groups ($n = 1$–10) on their pendant side chains. (B) Compressive modulus of Am-co-AA hydrogels (Am:AA = 7:1). Error bars indicate standard deviation. (C) Contact angle measurements of water droplets on 7:1 hydrogels with varying alkyl side chain lengths. The values are presented as mean ± standard deviation. (D) $4 \times 4\ \mu m^2$ AFM images of Am-co-AA hydrogels display flat surfaces with low roughness values. All images were acquired in PBS buffer using contact mode with triangular cantilevers of 0.06 N/m nominal spring constant. (E) Brightfield images of hMSCs on C1–C10 hydrogels and their quantification (F) after 24 h of plating. Error bars indicate standard deviation $P < 0.0001$, $n = 9$. Scale bars in $E = 400\ \mu m$ (G) Quantification of cell spreading on the hydrogels. Plot graphs display individual cell area measurements. Bars indicate the mean area for all measured cells. $P < 0.0001$, $n = 90$.

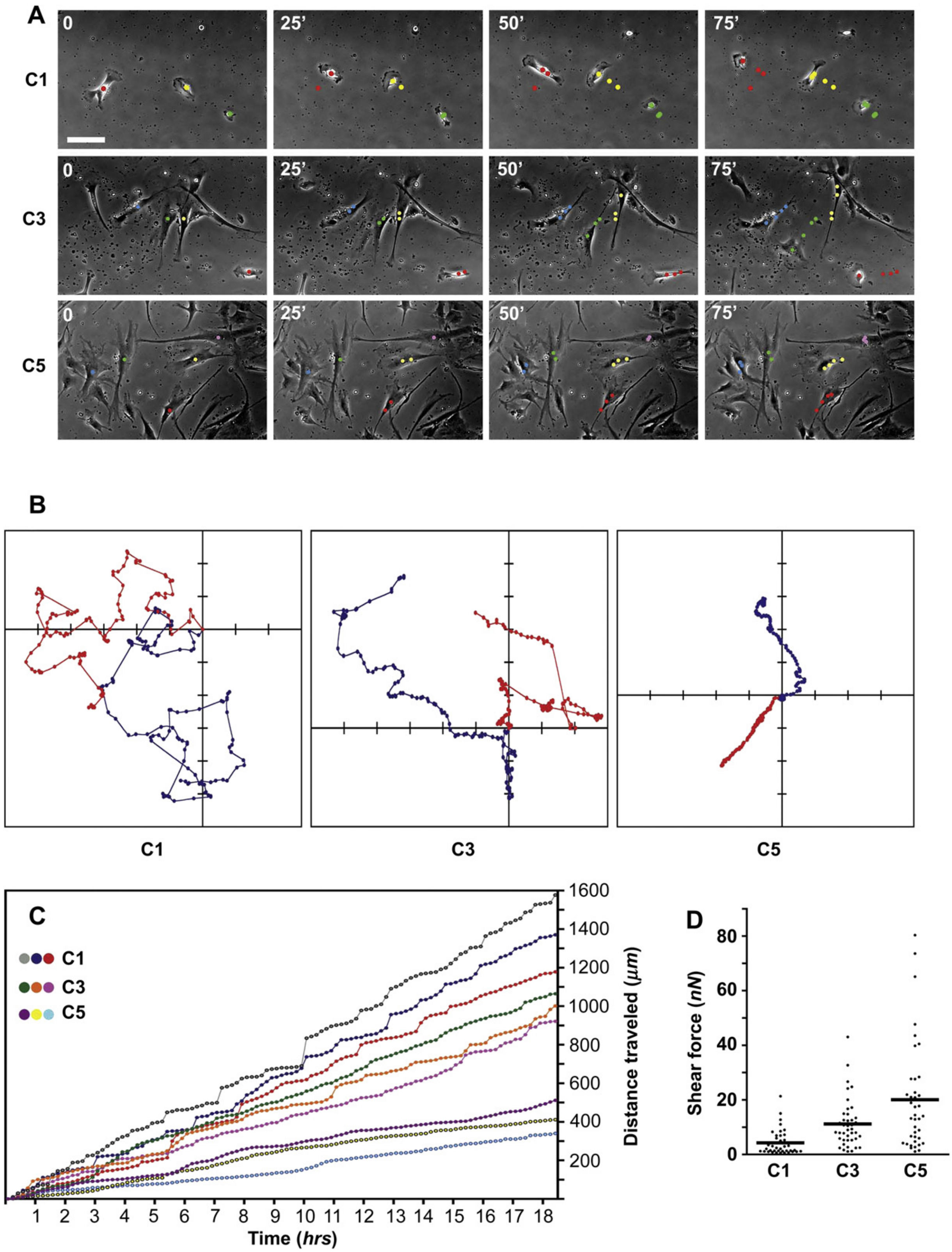

Fig. 2. Time-lapse video analysis of hMSC motility on C1, C3, and C5 hydrogels of 7:1 Am:AA. (A) Brightfield images of hMSCs taken every 25 min during a 75-min span. Colored dots track the position of the cell nuclei through all frames. Scale bar = 100 μm. (B) Graphical representation of cell displacements. The graphs trace the displacements of two representative cells (shown in red and blue) from each hydrogel over 19 h. Each dot represents the position of a few select cell nuclei at 10-min intervals relative to their position at time 0. Plot area for all graphs is 450 × 450 μm. Tick marks = 50 μm. (C) Traveled distance profile of three representative cells from each hydrogel. Each line indicates the total distance traveled by a cell over 19 h. Dots represent the distance traveled over a 10-min interval. (D) Shear forces required to detach cells from hydrogel matrices. Plot graphs display the individual cell measurements. Bars indicate the mean force for all measured cells. $P < 0.0001$; $n = 39$. (For interpretation of the references to colour in this figure legend, the reader is referred to the web version of this article).

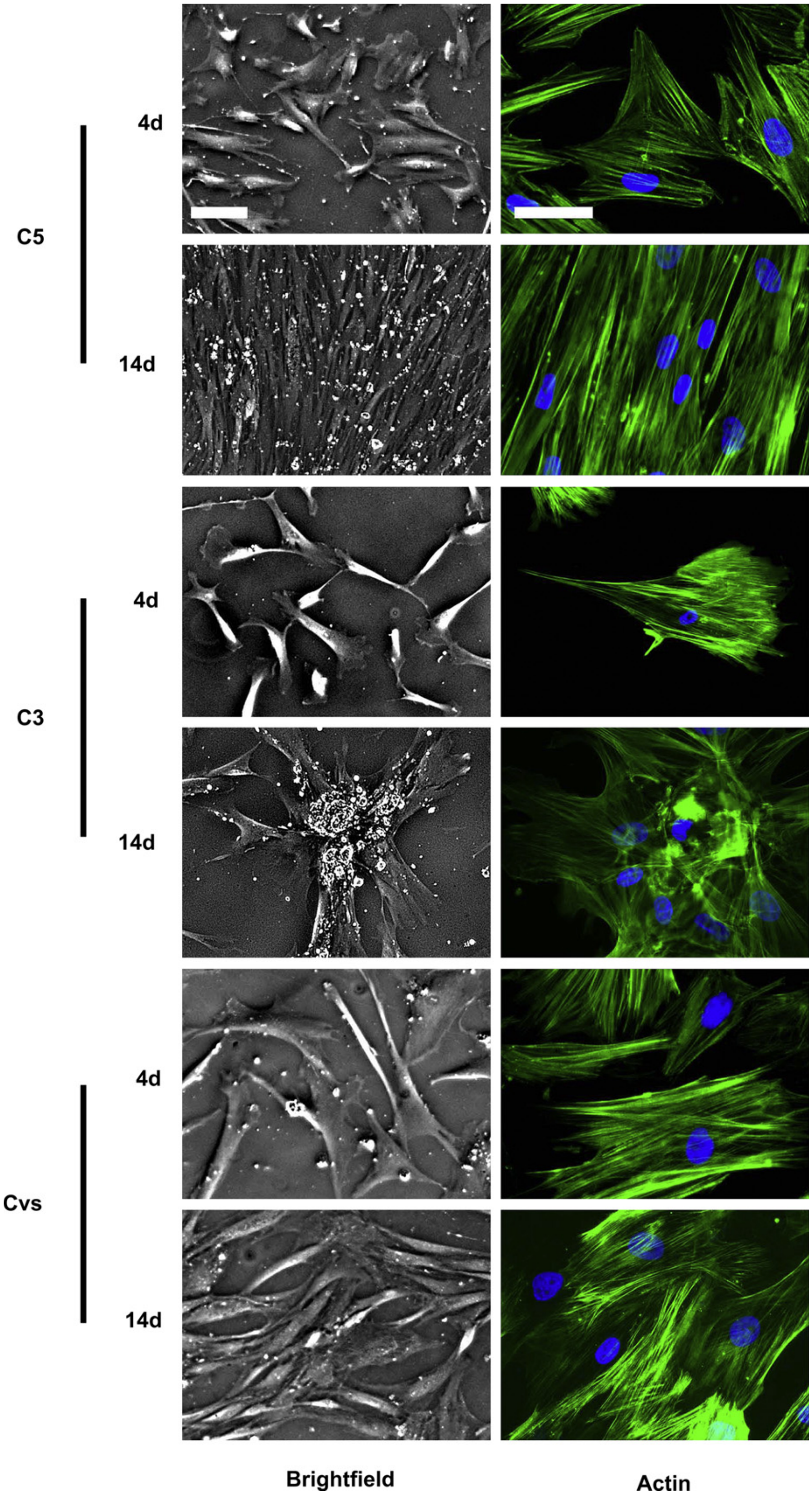

Fig. 3. C5 hydrogels promote hMSC organization. Brightfield (left column) and actin immunofluorescent staining (right column) of hMSCs on C3 and C5 hydrogels and glass coverslips (Cvs) after 4 and 14 days in culture. Scale bars = 100 μm (brightfield); 50 μm (immunofluorescence).

2.13. *Electrostatic calculations*

The electrostatic potentials for FN type-III repeats 7 through 10 and 12 through 14 were calculated by solving the linearized Poisson–Boltzmann equation (PBE) with the APBS package [26]. Coordinates for the two fragments of human FN encompassing type-III repeats 7 through 10 [27] and 12 through 14 [28] were obtained from the Protein Data Bank (PDB entries 1FNF and 1FNH, respectively). Hydrogen atoms were added to the crystal structures using PDB2PQR [29], and charges and radii were assigned according to PARSE force field parameters [30]. The electrostatic surface potential of the two fragments of FN was calculated by solving the linearized Poisson–Boltzmann equation (PBE) with the APBS [26] package. PBE calculations were performed at 310 K, using a 150 mM NaCl environment with solvent and solute dielectric constants of 2.0 and 78.5, respectively. APBS output including structures with 3D surface potentials was visualized using PyMol (www.pymol.org).

2.14. *Docking calculations*

Using the FN fragments described above as receptors, we utilized AutoDock Vina 1.0 [31] software to identify potential binding sites for the CH_3COO^- ligand. Polar hydrogen atoms and Gasteiger-Marsili charges [32] were added to FN, and CH_3COO^- was prepared through the same procedure. Default parameters were used as described in the manual with the exception of the maximum number of binding modes, which was set to 10,000. Binding modes within 1 kcal/mol of the most favorable binding free energy conformation (−3 kcal/mol) are shown in Fig. 6B.

2.15. *Osteogenic differentiation*

P4 hMSCs were cultured on C3 and C5 hydrogels and coverslips at a cell density of 5000 cells/cm^2 for 4 days in growth medium before changing into osteogenic medium (DMEM, 10% FBS, 50 μg/ml ascorbic acid, 10 mM β-glycerolphosphate, 10 nM dexamethasone and 50 units/ml penicillin/streptomycin) [33]. Cells were cultured under differentiating conditions for up to 21 days. Samples were collected at different time points for analysis. We denote day 0 time point as the day when the cells were switched to differentiating medium. In addition to cells cultured in osteogenic medium, we also characterized hMSCs cultured in growth medium (absence of osteogenic-inducing soluble factors) to understand matrix-mediated osteogenic differentiation.

2.16. *Myogenic differentiation*

P4 hMSCs were cultured on C3 and C5 hydrogels and coverslips at a cell density of 5000 cells/cm^2 for 7 days in growth medium, and then switched to myogenic medium (DMEM, 10 nM transferrin, 5 mg/ml insulin, 20 nM progesterone, 0.1 mM putrescine, 5.2 μg/ml selenite, 0.1 mM ascorbic acid-2-phosphate, 10 pM dexamethasone and 50 units/ml penicillin/streptomycin), and cultured for 21 days.

2.17. *Immunofluorescence*

Cells were fixed with 4% paraformaldehyde, washed in PBS, and blocked/permeabilized (3% bovine serum albumin, 0.1% triton X-100, in PBS) for 30 min. Cells were incubated with primary antibody, as labeled, diluted in blocking solution for 1 h at room temperature, washed in PBS, then incubated in Alexa Fluor 488-conjugated secondary antibodies (Invitrogen) diluted at 1:250 in blocking solution for 1 h at room temperature. In some instances, as labeled, Alexa Fluor 488-conjugated phalloidin (Invitrogen) was used, at 1:20 dilution, in blocking solution for 1 h at room temperature. Hydrogels were mounted with VectaShield-DAPI (Vector Laboratories), and imaged using a Zeiss Observer A1 microscope equipped with an X-Cite 120 (EXFO) mercury lamp. Primary antibodies: Osteocalcin, 1:100 (ab13420, Abcam); collagen I, 1:250 (70R-CR007X, Fitzgerald); desmin, 1:100 (ab15200, Abcam), myosin heavy chain, 1:100 (A4.1025, Developmental Hybridoma Bank); sarcomeric myosin heavy chain, 1:100 (MF-20, Developmental Hybridoma Bank).

2.18. *Alkaline phosphatase assay*

ALP staining was performed using Sigma Kit #85 (Sigma–Aldrich) per manufactures instructions [34]. In brief, cells were fixed in acetone/citrate solution, rinsed with water and stained with Fast Blue RR/naphthol.

2.19. *Alizarin red staining*

4% paraformaldehyde fixed cells were incubated for 30 min at room temperature in a 40 mM alizarin red solution (pH 4.1). Unincorporated dye was washed off with PBS.

2.20. *Real time and quantitative PCR*

Total RNA was extracted from three replicate samples with Trizol, and reverse-transcribed into cDNA using SuperScript First-Strand Synthesis System (Invitrogen). qRT-PCR reactions were performed using the SYBR Green PCR Mastermix and the ABI Prism 7700 Sequence Detection System (Perkin Elmer/Applied Biosystems, Rotkreuz, Switzerland) [34]. The cDNA samples were analyzed using β-actin as reference. The level of expression of each target gene is calculated as $2^{-\Delta\Delta Ct}$ [33]. The qRT-PCR products were separated by electrophoresis at 100 V on a 2% agarose gel in Tris–acetate–EDTA buffer and visualized after staining with ethydium bromide. The PCR primers are listed in Table S1.

2.21. *Statistical analysis*

One-way ANOVA with Bonferroni post-hoc analysis was used to analyze the data presented in Figs. 1 and 2, Fig. S4 and S5. A two-way ANOVA with Bonferroni post-hoc analysis was used to analyze the data presented in Figs. 4 and 5B.

3. Results

3.1. *Design of tunable matrices with varying hydrophobicity*

We have developed tunable synthetic matrices with precise control over their hydrophobicity by copolymerizing acrylamide (Am) with acryloyl amino acid (AA) monomers having dangling side chain of varying lengths, ranging from 1 to 10 CH_2 groups, terminating with a carboxyl group (Fig. 1A). These matrices are labeled C1, C2, …, C10 depending on the number of side chain CH_2 groups. The synthesis of AA monomers and hydrogels are confirmed by proton (^{1}H) and carbon (^{13}C) NMR spectroscopy (Figs. S1 and S2). Varying the number of side chain CH_2 groups, while maintaining the same molar ratio of Am to AA (e.g., 7 Am: 1 AA), permits us to modulate the surface hydrophobicity without altering the functional group, charge density, surface roughness, and bulk mechanical properties. The water contact angle measurements of the hydrogels confirm the increase in intrinsic hydrophobicity with increasing number of side chain CH_2 groups (Fig. 1C). Furthermore, we confirm that hydrogels of different hydrophobicity exhibit similar elastic modulus and surface roughness through compression tests and AFM imaging, respectively (Fig. 1B and D, and Fig. S3).

3.2. *Matrix hydrophobicity-mediated cell adhesion and proliferation of hMSCs*

Two hours post-plating of human bone marrow derived mesenchymal stem cells (hMSCs), it was clear that the incorporation of AA monomers increased the adhesive nature of the inherently bioinert Am hydrogels. However, significant differences in cell adhesion and spreading are noted amongst the various hydrogels, exhibiting a non-monotonic dependence on the length of the monomer side chain (Fig. S4, left). By 24 h, most cells (49.0 ± 2.6 cells/mm^2) adhere onto the C5 hydrogels. In contrast, less than half the cells adhere on C1, C7, or C10 hydrogels (25.6 ± 6.7, 22.7 ± 1.5, and 17.8 ± 0.6 cells/mm^2, respectively; Fig. 1E and F). The adhered cells proliferated on all the hydrogels, as noted from the ~1.5–2.5 fold increase in cell numbers after 4 days (Fig. S4C, left). Concomitant with the number of adherent cells, there are also marked changes in cell morphology and spreading (Fig. 1G and Fig. S4B, left). The few adherent cells on C1 hydrogels are either round or elongated with small lamellipodia (Fig. 1E). The surface area of these cells measure 2349 ± 94.2 μm^2 on average and never exceeds 5000 μm^2. Conversely, cells on the C5 hydrogels display larger surface areas (3000–13,000 μm^2; average 6427 ± 238.8 μm^2). Thus, side chains of 4–6 CH_2 groups seem ideal for cell adhesion and spreading.

Having established that a small amount of C5 monomer significantly enhances cell adhesion, we next investigated the effect of hydrogel composition by increasing the mole fraction of C5 moieties within the hydrogels: 7:1, 6:2, 5:3, and 3:5 (Fig. S5). Note that in cases where C5 content is increased (e.g. 3:5), the bulk mechanical and chemical properties are no longer invariant. The number of cells adhered to 6:2 hydrogels are similar to those on 7:1, but exhibit

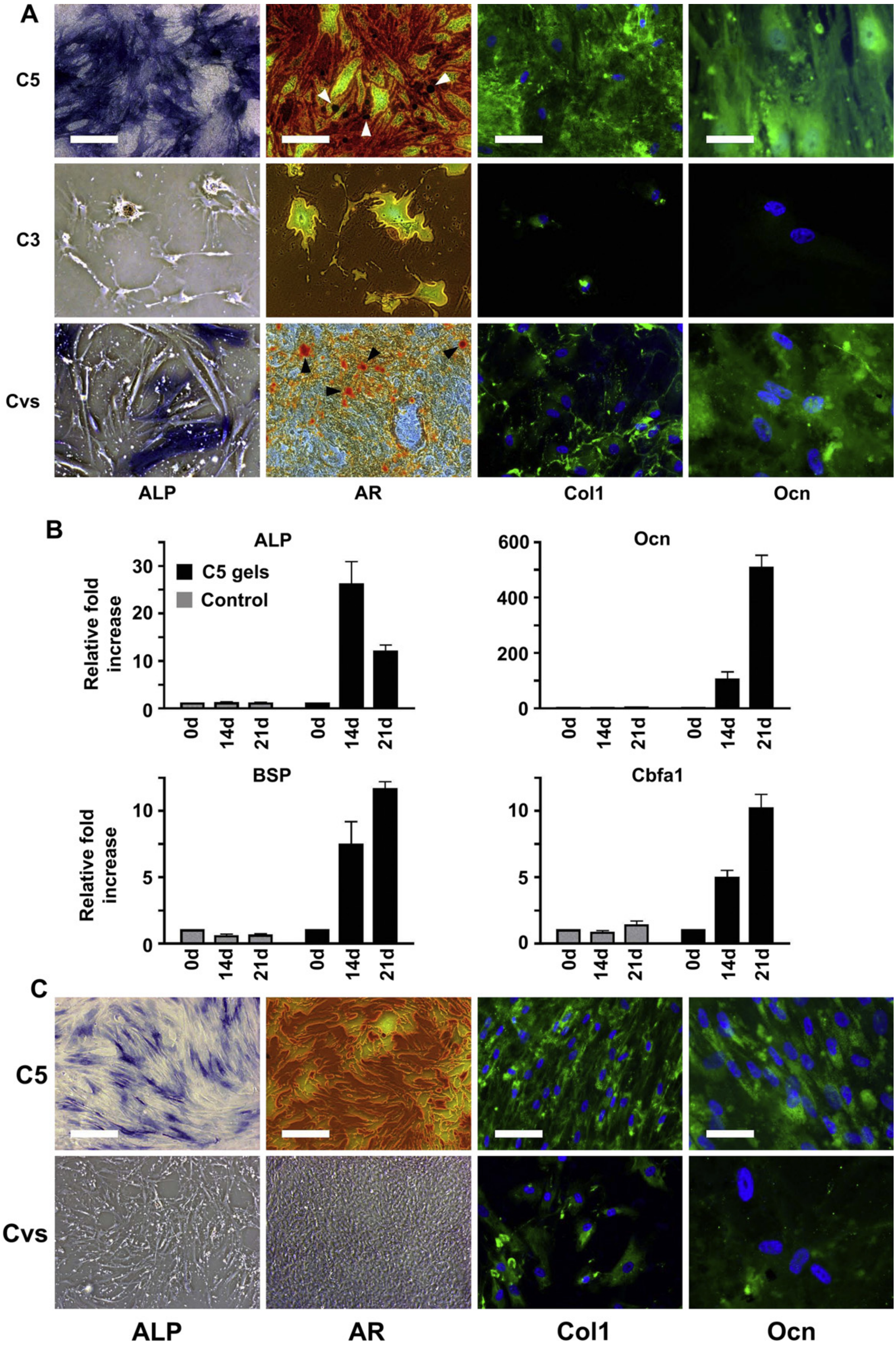

Fig. 4. Osteogenic differentiation of hMSCs. (A) Alkaline phosphatase (ALP) staining of hMSCs on C5 and C3 hydrogels and glass coverslips (Cvs) at 14 days in osteogenic medium; scale bar = 200 μm. Alizarin red S (AR) and immunofluorescent (green) staining for collagen I (Col1) and osteocalcin (Ocn) after 21 days. White (C5 hydrogels) and black (glass coverslips) arrowheads, in alizarin red S staining, point to calcium nodules. Nuclei in immunofluorescent stainings are labeled blue with DAPI. Scale bars = 100 μm (AR and collagen I) and 50 μm (Ocn). (B) Quantitative PCR of hMSCs cultured on C5 hydrogels or control (C3 hydrogels) for 14 or 21 days under osteogenic conditions. Plot graphs express "Relative fold expression"

a significant increase in cell spreading, averaging 9063 ± 331.0 μm^2 with some measuring >17,000 μm^2 (Figs. S4, right and S5). Surprisingly, further increase in C5 concentration (5:3, 3:5) results in a significant decrease in both cell adhesion and spreading.

3.3. Matrix hydrophobicity influences migration of hMSCs

Time-lapse video analysis of hMSCs on hydrogels corroborates the notable differences in cell morphology and spreading, while revealing contrasting differences in movement between C1 and C5 hydrogels, with cells on C3 hydrogels yielding an intermediate behavior (Fig. 2 and Movies S1–S3). On C1 hydrogels, cells continuously change their shape, often extending and contracting lamellipodia in multiple directions as if searching for a "sticky" site, then elongating in one direction before snapping back to a round morphology (which sometimes resulted in cell detachment) to begin the search process once again. Furthermore, cells often form multicellular clusters for extended periods of time before separating, indicating a preference for cell–cell interactions over cell–matrix interactions. In contrast, cells on C5 hydrogels display large, slowly evolving morphologies that rarely cluster despite high cell density.

Supplementary videos related to this article can be found at doi:10.1016/j.biomaterials.2011.02.004.

Graphic representations of the cellular movements reveal an erratic and random behavior with frequent directional changes for cells on C1 hydrogels, while cells on C5 hydrogels move in more deliberate and precise orientation (Fig. 2B). Also, the cells on C1 hydrogels travel significantly longer distances (1224.5 μm) averaging 1.11 μm/min and display "step-like" movements, compared to the smooth and slow (495.6 μm at 0.45 μm/min) movements observed on C5 hydrogels (Fig. 2C). Though the cells on C3 hydrogels are also somewhat erratic, they change direction less frequently and travel slower (1022.2 μm at 0.93 μm/min) than those on C1 hydrogels. These results are consistent with cell motility and migration speed being inversely proportional to cell surface area [6,35,36]. This is further confirmed by a shear-flow detachment assay where an average force of 20.1 ± 3.2 nN is needed to detach cells from C5 hydrogels, while the cells on C1 and C3 hydrogels only require 4.3 ± 0.8 and 11.2 ± 1.4 nN, respectively (Fig. 2D).

3.4. Matrix hydrophobicity influences cellular organization

Evaluation of long-term hMSC cultures reveals that C5 hydrogels provide an environment conducive for cell proliferation and migration, in accordance with their optimal adhesiveness. Surprisingly, these hMSCs (in growth medium) that lack orientation at earlier time points self-organize into a linear array as they reach confluency (Fig. 3). Such reorganization is also evident at the molecular level, as noted by the parallel, unidirectional organization of the actin cytoskeleton. This level of organization is in stark contrast to that of the less confluent hMSCs on C5 hydrogels, which show a spread, multidirectional actin cytoskeleton. Such cellular organization is unique to C5 hydrogels, as we do not observe it on other hydrogels or coverslips. Conversely, hMSCs on C3 hydrogels, which support cell survival and proliferation, tend to aggregate into large "rosette"-like clusters and maintain a fibroblastic morphology. Likewise, hMSCs grown on glass coverslips, while having similar morphology at low densities as those on C5 hydrogels, never attain the same degree of intracellular actin organization once they reach confluency (Fig. 3). The structural organization of the actin cytoskeleton is a direct response to cell–matrix and cell–cell interactions [4,35,37,38]; therefore, the organized arrangement of hMSCs speaks of highly coordinated cell–cell and cell–matrix interactions on C5 hydrogels.

3.5. Matrices with optimal hydrophobicity promote hMSCs differentiation

Cell–cell and cell–matrix interactions are known to play important roles in the differentiation commitment of stem cells through modulation of cell morphology and intracellular stress distribution [37,39–43]. We have taken advantage of the unique C5 hydrogel-mediated cytoskeletal organization to induce osteogenic and myogenic differentiation of hMSCs. We also compared the differentiation against corresponding C3 hydrogels and the widely used coverslips, though the properties of the coverslips are very different form the hydrogels.

At an initial cell density of 5000 cells/cm^2, hMSCs on C5 hydrogels exhibit spread morphology after 4 days of culture in growth medium (Fig. 3), which is more likely to undergo osteogenic differentiation [10,37,42]. Upon exposure to osteogenic medium, these cells undergo osteogenic differentiation, as characterized by gene and protein expressions (Fig. 4A and B). After 14 days of culture, alkaline phosphatase (ALP) activity and expression are detected in the hMSCs on C5 hydrogels while little and no activity is detected on coverslips and C3 hydrogels. In addition to the upregulation of osteogenic markers (Fig. 4B), hMSCs on C5 hydrogels stain positive for Alizarin red S (AR), collagen type 1, and osteocalcin (Fig. 4A). The AR staining reveals more calcium deposition and nodule formation on C5 hydrogels than on coverslips, and none on C3 hydrogels. Intense staining of osteocalcin and collagen type 1 is also observed on C5 hydrogels. Furthermore, hMSCs on C5 hydrogels undergo osteogenic differentiation even in the absence of any osteogenic-inducing soluble factors (Fig. 4C).

We also determine the ability of C5-mediated alignment of hMSCs on myogenic differentiation. The parallel arrangement of the actin cytoskeleton closely resembles that of myoblasts in culture and thereby may facilitate myogenic differentiation [10]. Indeed, these hMSCs cultured under myogenic conditions stain positive for desmin, MF20, and MHC (Fig. 5A) and also maintain higher expressions of myogenic markers such as MyoD, Myf5, and MHC (Fig. 5B). In contrast, cells on coverslips show minimal staining for MF20 and MHC. Surprisingly, while cells on C3 hydrogels show long-term survival and proliferation (~21 days) in growth medium, they undergo cell death when cultured in myogenic medium.

We also note that although the cells undergoing osteogenic differentiation continued to expand and become confluent they retain a spread morphology and random organization typical of osteoblasts, never aligning as under normal growth conditions (Figs. S6 and S7). On the other hand, the cells undergoing myogenic differentiation not only maintain their original aligned organization, but become longer and thinner, with a parallel actin filament cytoarchitecture reminiscent of myoblasts (Figs. S6 and S7).

normalized to 0 day expression (=1). Error bars denote standard deviation. Two-way ANOVA analysis: ALP, $P = 0.0002$ for interaction, $P < 0.0001$ for gel type, $P = 0.0002$ for time, $n = 3$; for all other markers, $P < 0.0001$ for interaction, gel type and time, $n = 3$. (C) ALP staining of hMSCs on C5 hydrogels and glass coverslips (Cvs) at 14 days in growth medium; scale bar = 200 μm. AR and immunofluorescent staining for Col1 after 21 days, and Ocn after 28 days. Nuclei in immunofluorescent stainings are labeled blue with DAPI. Scale bars = 100 μm (AR and Col1) and 50 μm (Ocn). (For interpretation of the references to colour in this figure legend, the reader is referred to the web version of this article).

3.6. Matrix hydrophobicity influences protein adsorption

Proteins at the cell–matrix interface play an important role on adhesion of cells onto synthetic matrices lacking cell surface binding ligands. The effect of matrix hydrophobicity on protein adsorption has been well documented [44–46], and its effect on cell adhesion has been demonstrated [45,47]. To dissect the role of proteins in regulating cell adhesion, we examine the proteins that selectively adsorb on 7:1 hydrogels with varying hydrophobicity. Western blot analysis reveals that the hydrogels selectively adsorb fibronectin (FN) and laminin (LN) from the serum (Fig. 6A) and other ECM proteins (vitronectin, collagen I, and fibrinogen) are absent. While little FN and LN are found on C1, C3, and C7 hydrogels, abundant protein is adsorbed on C5 hydrogels. This bell-shaped protein adsorption profile reflects the cell adhesion trend found on 7:1 hydrogels (Fig. 1F). The C5 monomer mediated protein adsorption is also evident in hydrogels with increasing C5 content; 3:5 C5 adsorbed more protein compared to the corresponding 7:1 hydrogels (Fig. 6A).

3.7. Reach and accessibility of hydrogel side chains determines protein adsorption

To understand the non-monotonic adsorption of FN and LN on hydrogels with varying hydrophobicity, we examine the binding of the AA alkyl side chains of the hydrogel to ECM proteins using FN as a model system. We first compute the electrostatic potential of two fragments of FN with known crystal structures: type-III repeats 7–10 [27] and 12–14 [28] (Fig. 6B). Other FN domains are not examined, as their structures are not known. Both fragments display multiple regions of positive and negative electrostatic potentials with the former acting as binding sites for the matrices' carboxyl groups, as confirmed by docking calculations of CH_3COO^- on the two fragments. The yellow spheres in Fig. 6B indicate the most favorable binding sites, with binding free energies between −2 and −3 kcal/mol. These sites are located in the positively charged pockets, where the van der Waals interactions are also strong. This observation, along with the expected atomic-level corrugation of the hydrogel surface, implies that the side chains must be sufficiently long to allow their terminal carboxyl groups to reach the binding sites on FN, thus explaining the small adsorption of FN on the surface of C1 hydrogels. As the chains become longer, the binding sites become more reachable, leading to increased adsorption.

The above argument, however, cannot explain the drop in adsorption observed on hydrogels with longer side chains (e.g., C7). To explain this effect, we hypothesize that the long side chains are highly hydrophobic and collapse onto the surface of the hydrogel, thus decreasing the accessibility of carboxyl groups for binding. We confirm this by computing the density of carboxyl groups in our hydrogel (∼0.1 M) and comparing it against solubility data of carboxylic acids [48] with varying hydrocarbon chain lengths (Fig. 6C). Short chains are completely soluble in water, but the solubility of chains larger than C4 decreases sharply with chain length. In fact, chains longer than C6 are no longer soluble in water

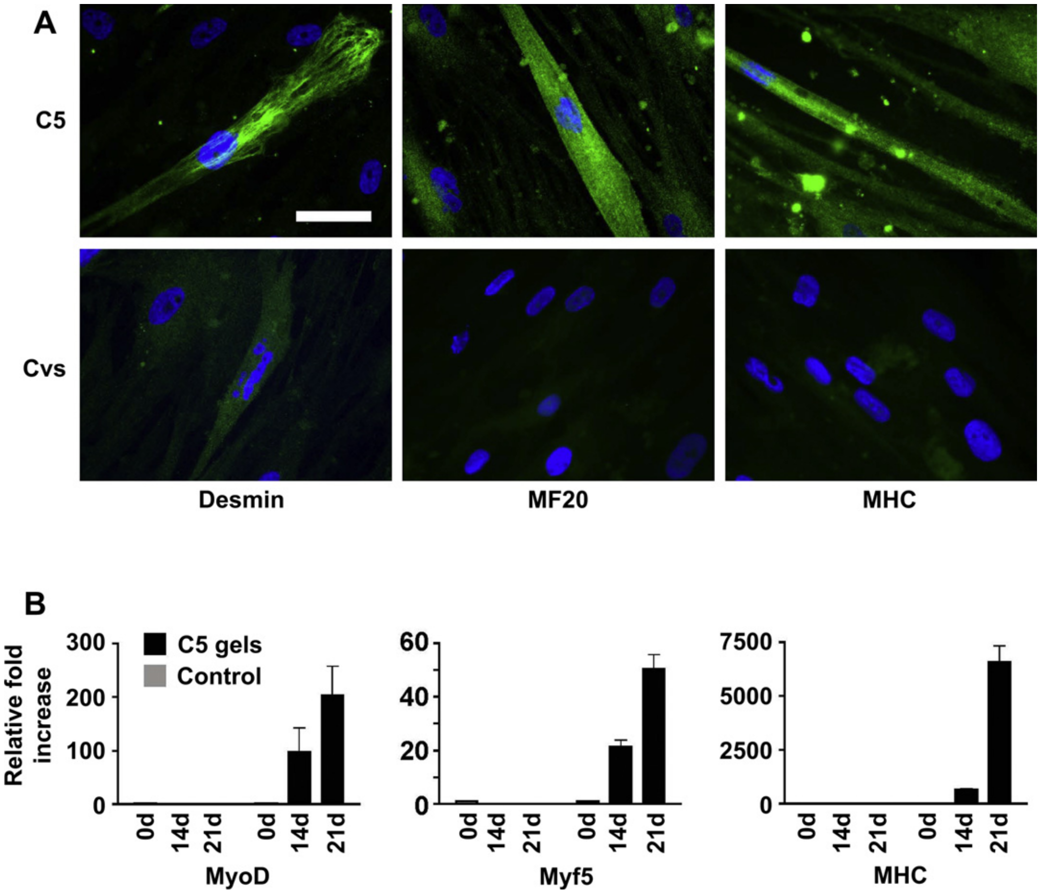

Fig. 5. Myogenic differentiation of hMSCs. (A) Immunofluorescent (green) staining of hMSCs cultured on C5 hydrogels or glass coverslips (Cvs) under myogenic conditions for 21 days. MHC, myosin heavy chain; MF-20, sarcomeric myosin heavy chain. Nuclei are labeled blue with DAPI. Scale bar = 50 μm. (B) Quantitative PCR of hMSCs cultured on C5 hydrogels or control (C3 hydrogels) for 14 or 21 days under myogenic conditions. Plot graphs express "Relative fold expression" normalized to 0 day expression (=1). Error bars denote standard deviation. Two-way ANOVA analysis: MyoD, $P = 0.0141$ for interaction, $P = 0.0011$ for gel type, $P = 0.015$ for time, $n = 3$; for all other markers, $P < 0.0001$ for interaction, gel type and time, $n = 3$. (For interpretation of the references to colour in this figure legend, the reader is referred to the web version of this article).

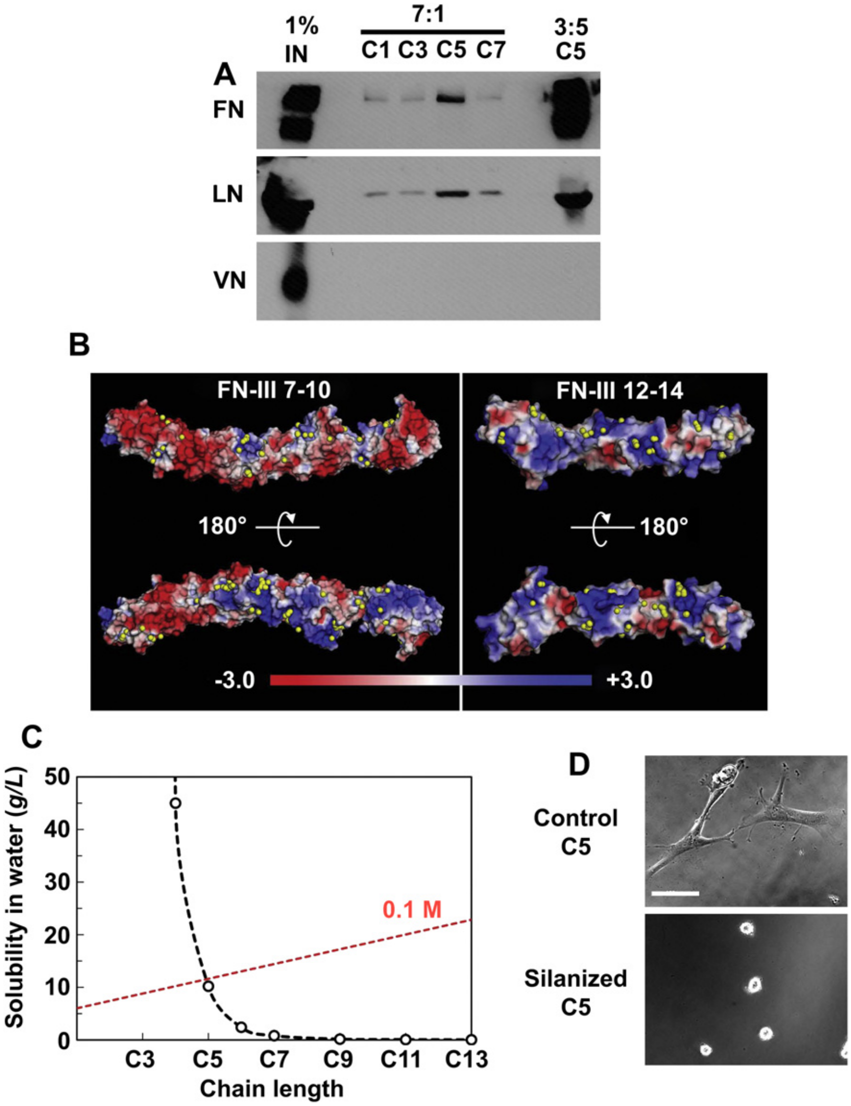

Fig. 6. Analyses of protein adsorption. (A) Western blot analysis of extracellular matrix proteins adsorbed on hydrogels with varying hydrophobicity. 1% IN: One percent of total fetal bovine serum incubated with hydrogels. (B) Electrostatic potential at the surface of FN-III 7–10 (left) and FN-III 12–14 (right) in eV computed using APBS. Red and blue colors indicate negative and positive potentials as dictated by the gradient bar at bottom. The yellow spheres represent the most favorable binding sites (−2 to −3 kcal/mol energies) for CH_3COO^- using Autodock. (C) Solubility data of carboxylic acids of varying hydrocarbon chain lengths in water (black circles). The dashed red line indicates the calculated density of carboxyl groups in our hydrogels. Regions above and below this line represent soluble and insoluble densities, respectively. (D) hMSCs cultured on standard C5 hydrogels and C5 hydrogels polymerized on silanized glass. Scale bar = 100 μm. (For interpretation of the references to colour in this figure legend, the reader is referred to the web version of this article).

at densities similar to those found in the hydrogels. This suggests that the side chains in C7 and C10 hydrogels likely collapse in a manner reminiscent of phase separation, rendering their terminal carboxyl groups inaccessible for binding. This argument is further supported by the significant reduction in cell adhesion observed when the side chains of the highly adhesive C5 hydrogels are forced to collapse (Fig. 6D).

To understand the poor cell adhesion and growth observed on 3:5 C5 hydrogels despite the large protein adsorption, we quantify the surface coverage of FN on 7:1 and 3:5 C5 hydrogels. Our western blot quantification shows that the 7:1 and 3:5 hydrogels adsorb 0.26 and 1.47 pmol/cm^2 of FN, respectively. These amounts translate to ~22% and ~124% surface coverage for the two hydrogels, respectively. These values are likely to be underestimated given that the adsorbed FN is highly impervious to detergent extraction [49]. We anticipate that the excess FN adsorbed on 3:5 C5 hydrogels results in a combination of conformational changes and steric inhibition [50], reducing their interaction with cell surface integrins and thus decreasing cell adhesion.

4. Discussion

This work demonstrates that small changes in matrix hydrophobicity through addition or deletion of CH_2 groups can dramatically alter cell–matrix interactions and in turn have a profound impact on various cellular behaviors such as adhesion, shape, motility, cytoskeletal organization, and differentiation. Another aspect of this study is the use of matrices that allow one to deconvolute the effects of matrix hydrophobicity from other effects arising from surface chemistry, surface topography, and mechanical properties of the matrices.

Interestingly, adhesion and spreading of hMSCs depend non-monotonically on matrix hydrophobicity, which correlates well with protein adsorption at the matrix interfaces with varying chain lengths but fixed composition. Our computational analyses reveal an intriguing mechanism for the observed bell-shaped protein adsorption profile. For short chains, the terminal carboxyl groups of AA side chains have limited reach to access FN binding sites, while for long chains, their hydrophobic collapse into the matrix results in decreased accessibility of carboxyl groups for binding.

The observed correlation between protein adsorption and cell adhesion is not surprising given that the adhesion is often mediated through proteins [45,47]. However, what is intriguing is that the protein adsorption alone could not support cell adhesion, as evident from the failure of 3:5 C5 hydrogels to support cell adhesion despite the large amount of proteins adsorbed. To our knowledge, very little data exists on the effects of super-saturated protein coverage on cell adhesion. Our surface coverage calculations of FN along with available literature [50–52] suggest that the excess adsorption of proteins could result in conformational changes and/or steric inhibition, thus limiting the interactions between the cell surface integrins and the underlying matrix. A number of studies have shown the influence of surface hydrophobicity and surface chemistry on conformation and assembly of proteins at the interface [51–53]. Taken together, our results imply that an optimal balance of hydrophobic–hydrophilic forces is required for promoting cell–matrix interactions.

We would like to point out that increasing the C5 content also increases the bulk rigidity of the hydrogels due to increase in osmotic pressure and repulsion between the charged carboxyl groups. However, the observed decrease in cell adhesion with increasing C5 content cannot be attributed to these changes in matrix rigidity, as it is well known that increasing rigidity leads to enhanced cell adhesion and spreading [10]. That we observe the contrary suggests that factors other than bulk mechanical properties are responsible for the observed effects.

In addition to modulating cell adhesion, hydrophobicity also influences the cytoskeletal organization of hMSCs in a cell-density dependent manner. Previous studies have shown that the cytoskeletal changes that stem cells undergo responding to their extrinsic/intrinsic cues can direct their differentiation commitment [10,37,39,43]. By harnessing the changes in cytoskeletal organization of hMSCs on C5 hydrogels, we were able to direct their differentiation into both myogenic and osteogenic lineages. Interestingly, the C5 hydrogels could promote osteogenic differentiation even in the absence of osteogenic-inducing factors.

Furthermore, even though the adhered cells on C3 hydrogels exhibited long-term growth, they not only failed to differentiate, but underwent cell death in myogenic differentiation conditions. This suggests the plausible requirement of strong cell–matrix adhesion to support the cytoskeletal rearrangements and intracellular tensions that the stem cells undergo during differentiation. Such interplay between matrix adhesivity and cell-generated tension on the function of cells has been demonstrated previously using differentiated cells [5,54,55].

5. Conclusions

This study advances our understanding of how interfacial modulation of the extracellular matrix, which occurs both in tissue formation and disease progression, can play a considerably larger role in dictating cellular behaviors than previously envisioned. Ultimately, such an understanding of matrix interface-mediated adhesion, migration, and differentiation of stem cells could have implications in regenerative medicine. Moreover, the tunable matrices developed here introduce a new control parameter for regulating various cellular functions, thus offering a platform for studying proliferation and lineage specificity of stem cells in a controlled manner.

Author contributions

R.A. and S.V. designed the experiments and interpreted the data. R.A., S.V., and G.A. wrote the manuscript. R.A. performed the cell experiments. C.Z. synthesized and characterized the monomers. D.Y. and G.A. performed the computational analysis. A.A. carried out the shear force analysis. Y.H. conducted the contact angle measurements. S.S.S., F.T.A., and R.L. carried out AFM analysis.

Acknowledgments

We thank Dr. Jeff Hasty and Martin Kolnik for their help on time-lapse microscopy, Drs. Shu Chien and Julie Li for providing the flow chamber used in the shear flow experiments, Dr. Anthony Mrse for his assistance in NMR measurements, Drs. Marc Meyers and Yasuaki Seki for help in mechanical tests, and Dr. Sungho Jin for contact angle measurements. This work was supported by the California Institute of Regenerative Medicine (#RN2-00945-1) and the NIH Training Grant (#2T32 HL-007089). The hMSCs used in this study were provided by the Tulane Center for Gene Therapy through a grant from NCRR of the NIH (#P40RR017447).

Appendix. Supplementary material

The supplementary data associated with this article can be found in the on-line version at doi:10.1016/j.biomaterials.2011.02.004.

References

[1] Carter SB. Haptotaxis and the mechanism of cell motility. Nature 1967;213:256–60.
[2] Fuchs E, Tumbar T, Guasch G. Socializing with the neighbors: stem cells and their niche. Cell 2004;116:769–78.
[3] Folkman J, Moscona A. Role of cell shape in growth control. Nature 1978;273:345–9.
[4] Gumbiner BM. Cell adhesion: the molecular basis of tissue architecture and morphogenesis. Cell 1996;84:345–57.
[5] Berrier AL, Yamada KM. Cell-matrix adhesion. J Cell Physiol 2007;213:565–73.
[6] Palecek SP, Loftus JC, Ginsberg MH, Lauffenburger DA, Horwitz AF. Integrin-ligand binding properties govern cell migration speed through cell-substratum adhesiveness. Nature 1997;385:537–40.
[7] Guilak F, Cohen DM, Estes BT, Gimble JM, Liedtke W, Chen CS. Control of stem cell fate by physical interactions with the extracellular matrix. Cell Stem Cell. 2009;5:17–26.
[8] Harris A. Behavior of cultured cells on substrata of variable adhesiveness. Exp Cell Res 1973;77:285–97.
[9] Lutolf MP, Hubbell JA. Synthetic biomaterials as instructive extracellular microenvironments for morphogenesis in tissue engineering. Nat Biotechnol 2005;23:47–55.
[10] Engler AJ, Sen S, Sweeney HL, Discher DE. Matrix elasticity directs stem cell lineage specification. Cell 2006;126:677–89.
[11] Burdick JA, Vunjak-Novakovic G. Engineered microenvironments for controlled stem cell differentiation. Tissue Eng Part A 2009;15:205–19.
[12] Benoit DS, Schwartz MP, Durney AR, Anseth KS. Small functional groups for controlled differentiation of hydrogel-encapsulated human mesenchymal stem cells. Nat Mater 2008;7:816–23.
[13] Phillips JE, Petrie TA, Creighton FP, Garcia AJ. Human mesenchymal stem cell differentiation on self-assembled monolayers presenting different surface chemistries. Acta Biomater 2010;6:12–20.
[14] Huebsch N, Arany PR, Mao AS, Shvartsman D, Ali OA, Bencherif SA, et al. Harnessing traction-mediated manipulation of the cell/matrix interface to control stem-cell fate. Nat Mater 2010;9:518–26.
[15] Mei Y, Saha K, Bogatyrev SR, Yang J, Hook AL, Kalcioglu ZI, et al. Combinatorial development of biomaterials for clonal growth of human pluripotent stem cells. Nat Mater 2010;9:768–78.
[16] Thomson D. On growth and form. New York: Cambridge University Press; 1961.
[17] Lecuit T, Lenne PF. Cell surface mechanics and the control of cell shape, tissue patterns and morphogenesis. Nat Rev Mol Cell Biol 2007;8:633–44.
[18] Liotta LA, Kohn EC. The microenvironment of the tumour-host interface. Nature 2001;411:375–9.
[19] Chen YM, Gong JP, Tanaka M, Yasuda K, Yamamoto S, Shimomura M, et al. Tuning of cell proliferation on tough gels by critical charge effect. J Biomed Mater Res A 2009;88:74–83.

[20] Stevens MM, George JH. Exploring and engineering the cell surface interface. Science 2005;310:1135–8.

[21] Dalby MJ, Gadegaard N, Tare R, Andar A, Riehle MO, Herzyk P, et al. The control of human mesenchymal cell differentiation using nanoscale symmetry and disorder. Nat Mater 2007;6:997–1003.

[22] Dill KA. Dominant forces in protein folding. Biochemistry 1990;29:7133–55.

[23] Kauzmann W. Some factors in the interpretation of protein denaturation. Adv Protein Chem 1959;14:1–63.

[24] Badiger MV, Lele AK, Bhalerao VS, Varghese S, Mashelkar RA. Molecular tailoring of thermoreversible copolymer gels: some new mechanistic insights. J Chem Phys 1998;109:1175–84.

[25] Zhang C, Aung A, Liao LQ, Varghese S. A novel single precursor-based biodegradable hydrogel with enhanced mechanical properties. Soft Matter 2009;5:3831–4.

[26] Baker NA, Sept D, Joseph S, Holst MJ, McCammon JA. Electrostatics of nanosystems: application to microtubules and the ribosome. Proc Natl Acad Sci U S A 2001;98:10037–41.

[27] Leahy DJ, Aukhil I, Erickson HP. 2.0 A crystal structure of a four-domain segment of human fibronectin encompassing the RGD loop and synergy region. Cell 1996;84:155–64.

[28] Sharma A, Askari JA, Humphries MJ, Jones EY, Stuart DI. Crystal structure of a heparin- and integrin-binding segment of human fibronectin. Embo J 1999; 18:1468–79.

[29] Dolinsky TJ, Nielsen JE, McCammon JA, Baker NA. PDB2PQR: an automated pipeline for the setup of Poisson–Boltzmann electrostatics calculations. Nucleic Acids Res 2004;32:W665–7.

[30] Sitkoff D, Sharp KA, Honig B. Accurate calculation of hydration free energies using macroscopic solvent models. J Phys Chem 1994;98:1978–88.

[31] Trott O, Olson AJ. AutoDock Vina: improving the speed and accuracy of docking with a new scoring function, efficient optimization, and multithreading. J Comput Chem 2010;31:455–61.

[32] Gasteiger J, Marsili M. Iterative partial equalization of orbital electronegativity-a rapid access to atomic charges. Tetrahedron 1980;36:3219–28.

[33] Varghese S, Hwang NS, Ferran A, Hillel A, Theprungsirikul P, Canver AC, et al. Engineering musculoskeletal tissues with human embryonic germ cell derivatives. Stem Cells 2010;28:765–74.

[34] Hwang NS, Varghese S, Lee HJ, Zhang Z, Ye Z, Bae J, et al. In vivo commitment and functional tissue regeneration using human embryonic stem cell-derived mesenchymal cells. Proc Natl Acad Sci U S A 2008;105:20641–6.

[35] Yeung T, Georges PC, Flanagan LA, Marg B, Ortiz M, Funaki M, et al. Effects of substrate stiffness on cell morphology, cytoskeletal structure, and adhesion. Cell Motil Cytoskeleton 2005;60:24–34.

[36] Gail MH, Boone CW. Cell-substrate adhesivity. A determinant of cell motility. Exp Cell Res 1972;70:33–40.

[37] McBeath R, Pirone D, Nelson C, Bhadriraju K, Chen C. Cell shape, cytoskeletal tension, and RhoA regulate stem cell lineage commitment. Dev Cell 2004; 6:483–95.

[38] Turner DC. Cell-cell and cell-matrix interactions in the morphogenesis of skeletal muscle. Dev Biol (N Y 1985) 1986;3:205–24.

[39] Connelly JT, Gautrot JE, Trappmann B, Tan DW, Donati G, Huck WT, et al. Actin and serum response factor transduce physical cues from the microenvironment to regulate epidermal stem cell fate decisions. Nat Cell Biol 2010; 12:711–8.

[40] Wang N, Ingber DE. Control of cytoskeletal mechanics by extracellular matrix, cell shape, and mechanical tension. Biophys J 1994;66:2181–9.

[41] Ingber DE. Cellular tensegrity: defining new rules of biological design that govern the cytoskeleton. J Cell Sci 1993;104(Pt 3):613–27.

[42] Guvendiren M, Burdick JA. The control of stem cell morphology and differentiation by hydrogel surface wrinkles. Biomaterials 2010;31:6511–8.

[43] Treiser MD, Yang EH, Gordonov S, Cohen DM, Androulakis IP, Kohn J, et al. Cytoskeleton-based forecasting of stem cell lineage fates. Proc Natl Acad Sci U S A 2010;107:610–5.

[44] Wu Y, Simonovsky FI, Ratner BD, Horbett TA. The role of adsorbed fibrinogen in platelet adhesion to polyurethane surfaces: a comparison of surface hydrophobicity, protein adsorption, monoclonal antibody binding, and platelet adhesion. J Biomed Mater Res A 2005;74:722–38.

[45] Tidwell CD, Ertel SI, Ratner BD, Tarasevich BJ, Atre S, Allara DL. Endothelial cell growth and protein adsorption on terminally functionalized, self-assembled monolayers of alkanethiolates on gold. Langmuir 1997;13:3404–13.

[46] Prime K, Whitesides G. Self-assembled organic monolayers: model systems for studying adsorption of proteins at surfaces. Science 1991;252:1164–7.

[47] Nuttelman CR, Mortisen DJ, Henry SM, Anseth KS. Attachment of fibronectin to poly(vinyl alcohol) hydrogels promotes NIH3T3 cell adhesion, proliferation, and migration. J Biomed Mater Res 2001;57:217–23.

[48] Lide D. Handbook of chemistry and physics. CRC; 2008–2009.

[49] Grinnell F, Feld MK. Adsorption characteristics of plasma fibronectin in relationship to biological activity. J Biomed Mater Res 1981;15:363–81.

[50] Pernodet N, Rafailovich M, Sokolov J, Xu D, Yang NL, McLeod K. Fibronectin fibrillogenesis on sulfonated polystyrene surfaces. J Biomed Mater Res A 2003;64:684–92.

[51] Michael KE, Vernekar VN, Keselowsky BG, Meredith JC, Latour RA, Garcia AJ. Adsorption-induced conformational changes in fibronectin due to interactions with well-defined surface chemistries. Langmuir 2003;19:8033–40.

[52] Coelho NM, Gonzalez-Garcia C, Planell JA, Salmeron-Sanchez M, Altankov G. Different assembly of type IV collagen on hydrophilic and hydrophobic substrata alters endothelial cells interaction. Eur Cell Mater 2010;19:262–72.

[53] Keselowsky BG, Collard DM, Garcia AJ. Surface chemistry modulates fibronectin conformation and directs integrin binding and specificity to control cell adhesion. J Biomed Mater Res A 2003;66:247–59.

[54] Ben-Ze'ev A, Farmer SR, Penman S. Protein synthesis requires cell-surface contact while nuclear events respond to cell shape in anchorage-dependent fibroblasts. Cell 1980;21:365–72.

[55] Ingber DE. Fibronectin controls capillary endothelial cell growth by modulating cell shape. Proc Natl Acad Sci U S A 1990;87:3579–83.